RECONSTRUCTION OF PARTIALLY SAMPLED EELS IMAGES

Etienne Monier[1], Thomas Oberlin[1], Nathalie Brun[2], Marcel Tencé[2], Maria de Frutos[2] and Nicolas Dobigeon[1]

[1] University of Toulouse, IRIT/INP-ENSEEIHT, 31071 Toulouse Cedex 7, France
[2] LPS, CNRS UMR 8502, Univ. Paris-Sud, Univ. Paris-Saclay, 91405 Orsay Cedex, France

ABSTRACT

Electron microscopy has shown to be a very powerful tool to deeply analyze the chemical composition at various scales. However, many samples can not be analyzed with an acceptable signal-to-noise ratio because of the radiation damage induced by the electron beam. Particularly, electron energy loss spectroscopy (EELS) which acquires a spectrum for each spatial position requires high beam intensity. Scanning transmission electron microscopes (STEM) sequentially acquire data cubes by scanning the electron probe over the sample and record a spectrum for each spatial position. Recent works developed new acquisition procedures, which allow for partial acquisition schemes following a predetermined scan pattern. A reconstruction of the full data cube is conducted as a post-processing step. A multi-band image reconstruction procedure which exploits the spectral structure and the spatial smoothness of STEM-EELS images is explained here. The performance of the proposed scheme is illustrated thanks to experiments conducted on a realistic phantom dataset as well as real EELS spectrum-image.

Index Terms— Electron Energy Loss Spectroscopy EELS, Scanning Transmission Electron Microscope STEM, spectrum-image, multi-band imaging, image reconstruction, partial sampling, inpainting.

1. INTRODUCTION

In a scanning transmission electron microscope (STEM), an electron beam is used as the illumination source and is focused as a probe which is moved over the sample area of interest. Among the commonly collected signals is the electron-energy loss spectrum (EELS) [1] which is multi-channels (the acquired multi-band image is called a spectrum-image). However, a classical problem encountered is that the electron beam induce damages for sensitive materials [2] such as organic materials. Indeed, standard acquisition schemes operate sequentially, line-by-line, and thus concentrate electrons in contiguous areas. Common solution consists in reducing the electron dose (number of electrons per unit surface), which significantly lowers the signal-to-noise ratio (SNR) and the overall image quality. Recent works proposed another approach which consists in a random sampling scheme for reducing cumulative damage on successive pixels while keeping the best SNR and spatial resolution [3]. The last method has several advantages as it allows adaptive studies to be envisioned. Such a random sampling has been implemented on the STEM VG HB 501 microscope in the Laboratoire de Physique des Solides (LPS, Orsay, France) [4].

Our approach is based on a partial and random acquisition scheme, with optimal electron dose per pixel compared to full acquisition schemes with a reduced dose. This partial acquisition improves significantly the SNR for the sampled areas. It requires computational reconstruction schemes to recover the full data from the partial measurements within a post-processing task. In image processing this is commonly referred to as inpainting, a particular inverse problem which can be solved by means of appropriate spatial and spectral regularizations. Besides, the acquisition scan pattern, which can be chosen before the acquisition, should be studied as it impacts the reconstruction quality.

This paper considers the reconstruction of EELS spectrum-images from partial acquisition. An optimization problem introducing a spatial regularization, chosen to promote smoothly varying images, *and* a spectral regularization to better take into account the nature of EELS data is proposed for a reconstruction task. The choice of the scan pattern is also discussed. Section 2 formulates the problem and develops the proposed method. Section 3 describes its implementation and presents the scan patterns that will be compared. This approach will be evaluated with numerical simulations conducted on a realistic image in section 4, while Section 5 reports experiments on a real dataset acquired by the STEM VG HB 501 microscope operated by LPS. Section 6 finally concludes this work.

2. PROPOSED METHOD

2.1. Direct and inverse problem

Let $\mathbf{Y}$ denote the $M \times P$ matrix that corresponds to the full EELS data composed of P pixels in M channels. To avoid

Part of this work has been funded by CNRS, France, through the Imag'in ARSIS project and the METSA 17A304 program.

the damaging effects the electron dose could have on sensitive samples, only some given spatial locations are acquired. Note that this spatial subsampling scheme is not accompanied by any spectral subsampling, since, at each spatial position, the EELS spectrometer simultaneously separates all electron loss energies, leading to the acquisition of the whole EELS spectrum. To summarize, the full spectra are acquired at N among P available spatial positions, resulting in the spatial subsampling ratio $r = N/P$. The corresponding index set of the N acquired pixels and the matrix of the measurements gathering the N columns of $\mathbf{Y}$ are denoted $\mathcal{I}$ and $\mathbf{Y}_{\mathcal{I}}$, respectively.

Multiband images encountered in numerous imaging modalities are known to be highly spectrally correlated and, in most cases, obey a low-rank property. A physically-motivated instance of this property arises when analyzing multi-band images under the unmixing paradigm [5]. We exploit this property through dimension reduction, which also allows for lighter computations. More precisely, the image to be recovered is assumed to write $\mathbf{X} = \mathbf{HS}$ where $\mathbf{H}$ is a $M \times M$ orthonormal matrix defining the data principal component basis and $\mathbf{S} = [\mathbf{s}_1, \ldots, \mathbf{s}_P]$ is a $M \times P$ matrix which gathers the representation coefficients of the spectrum-pixels in this basis. In this work, the basis $\mathbf{H}$ is supposed to be estimated beforehand by conducting a principal component analysis (PCA) of the observed pixels $\mathbf{Y}_{\mathcal{I}}$. Note that, as discussed in Section 1, a partial spatial sampling of the scene results in a higher SNR than the one obtained with a conventional sampling. Thus, the first principal components of highest energy are expected to span a reliable estimate of the actual signal subspace (assumed to be of dimension R_{true}).

Given this decomposition, the reconstruction problem, which consists in recovering a full (and possibly denoised) $M \times P$ spectrum-image $\mathbf{X}$ from the acquired data $\mathbf{Y}_{\mathcal{I}}$, can be formulated directly into the principal component basis and boils down to estimating the $M \times P$ coefficient matrix $\mathbf{S}$. This reconstruction task is an ill-posed problem and can be addressed by solving the following optimization problem

$$\begin{aligned} \hat{\mathbf{S}} &= \underset{\mathbf{S} \in \mathbb{R}^{M \times P}}{\arg\min}\ \phi(\mathbf{S}) + \mu\psi(\mathbf{S}) \\ &\text{s.t.} \quad \frac{1}{M} \left\| \mathbf{H}^T \mathbf{Y}_{\mathcal{I}(n)} - \mathbf{S}_{\mathcal{I}(n)} \right\|_2^2 \leq \hat{\sigma}^2,\ \forall n \in [\![1, M]\!] \end{aligned} \quad (1)$$

where $\phi(\cdot)$ and $\psi(\cdot)$ are spatial and spectral regularizations with μ a parameter adjusting their relative impact. The data fitting term is written as a constraint, since the squared Euclidean distance between the observations and the solution is expected to be equal to noise variance σ whose estimation is $\hat{\sigma}$ because we assume independent white Gaussian noise. The resulting proposed method will be referred to as Sobolev SubSpace (3S).

2.2. The spatial regularization

Classical spatial regularizations used in image restoration usually rely on the image gradient $\mathbf{XD}$, where $\mathbf{D}$ is the spatial discrete gradient operator applied in each channel independently. This gradient is minimized with respect to (w.r.t.) its ℓ_2-norm to promote smoothly varying image. Here, the EELS images are expected to be spatially smooth since the target spatial resolution is relatively low compared to the atomic resolution. As a consequence, the energy of the spatial gradient, which enforces spatial smoothness in each band, will be considered

$$\phi(\mathbf{S}) = \frac{1}{2M} \left\| \mathbf{SD} \right\|_{\text{F}}^2 . \quad (2)$$

2.3. The spectral regularization

When the eigenvectors $\mathbf{h}_1, \ldots, \mathbf{h}_M$ identified by PCA and composing the columns of $\mathbf{H}$ are ordered such that the eigenvalues are sorted in decreasing order, the corresponding representation vectors $\mathbf{S}_{1,:}, \ldots, \mathbf{S}_{M,:}$ are expected to be of decreasing energy magnitudes, where $\mathbf{S}_{m,:}$ stands for the mth row of $\mathbf{S}$. In particular, if the pixel spectra lie into a subspace of dimension R_{true} with $R_{\text{true}} \leq M$, the squared norms $\|\mathbf{S}_{m,:}\|_2^2$ of the irrelevant representation vectors are expected to be close to 0 for $m \geq R_{\text{true}}$. This suggests a weighted penalization of the form

$$\psi(\mathbf{S}) = \frac{1}{2} \sum_{m=1}^{M} \mathbf{w}_m \left\| \mathbf{S}_{m,:} \right\|_2^2 \quad (3)$$

with increasing weights $(\mathbf{w}_m)_{m=1,\ldots,M}$. A Bayesian interpretation yields to the following formulation [6]

$$\mathbf{w}_m = \frac{\hat{\sigma}^2}{l_m - \hat{\sigma}^2} \quad (4)$$

with $(l)_{m=1,\ldots,M}$ the estimated eigenvalues of the spectrum image covariance matrix. We consider the following Stein estimator

$$l_m = \frac{\lambda_m}{1 + \frac{1}{N} \sum_{\substack{j=1 \\ j \neq m}}^{M} \frac{\lambda_m + \lambda_j}{\lambda_m - \lambda_j}} \quad (5)$$

where $(\lambda)_{m=1,\ldots,M}$ are the PCA eigenvalues ordered in decreasing order. An isotonic regression [7] is used as a post-processing to ensure the non-decreasing property of $(l)_{m=1,\ldots,M}$, which usually returns a set of corrected eigenvalues with associated multiplicity orders. Moreover, an estimate $\hat{\sigma}^2$ of the noise variance can be chosen as the corrected eigenvalues of lowest magnitude, whose multiplicity order is expected to be $M - R$. Hence, for $m > R$, $\mathbf{S}_{m,:}$ is forced to be null. In other words, the optimization problem (1) can be equivalently rewritten with respect to a $R \times P$ matrix $\mathbf{S}_{1:R,:}$ and where all the occurrences of M are replaced by R.

3. IMPLEMENTATION

3.1. Optimization

The optimization problem (1) amounts to minimizing the sum of the following functions

$$f(\mathbf{S}) = \phi(\mathbf{S}) + \mu\psi(\mathbf{S}) \tag{6}$$

$$g(\mathbf{S}) = \sum_{n=1}^{N} \iota_{\mathcal{B}(\mathbf{H}^T\mathbf{Y}_{\mathcal{I}(n)}, \sqrt{R}\hat{\sigma})}(\mathbf{S}_{\mathcal{I}(n)}) \tag{7}$$

where $\iota_{\mathcal{A}}(x)$ is the indicator function of a set $\mathcal{A}$ and $\mathcal{B}(x_0, r_0)$ is the ball centered on x_0 of radius r_0. Using this decomposition, f is a convex and continuously differentiable function with L_f-Lipschitz continuous gradient (with $L_f \leq L_{UB} = 1 + 8\mu$) and g is a convex nonsmooth function. Hence, for all $L \geq L_f$ (particularly, for $L = L_{UB}$), the FISTA algorithm [8] given in Algo. 1 converges toward the solution of our optimization problem.

The corresponding gradient of $f(\cdot)$ required in Step 3 of Algo. 1 is given by

$$\nabla f(\mathbf{S}) = -\frac{1}{R}\mathbf{S}\Delta + \mu\mathbf{W}\mathbf{S} \tag{8}$$

where $\Delta = -\mathbf{D}\mathbf{D}^T$ is the discrete spatial Laplacian operator. Moreover, as shown by (7), the function $g(\cdot)$ is separable with respect to the pixel indexes $n \in [\![1, N]\!]$. Hence, the proximal operator associated with $g(\cdot)$ consists in projecting $\mathbf{S}_{\mathcal{I}(n)}$ on $\mathcal{B}(\mathbf{H}^T\mathbf{Y}_{\mathcal{I}(n)}, \sqrt{R}\hat{\sigma})$ for all $n \in [\![1, N]\!]$.

Algorithm 1: FISTA with constant step size [8]

Input : $L > L_f$ an upper bound of L_f

Initialisation : Set $\mathbf{y}^{(1)} = \mathbf{x}^{(0)} \in \mathbb{R}^p$, $\theta^{(1)} = 1$, $i = 1$

while *stopping rule not satisfied* **do**

- $\mathbf{x}^{(i)} = \text{prox}_{g/L}\left(\mathbf{y}^{(i)} - \frac{1}{L}\nabla f(\mathbf{y}^{(i)})\right)$
- $\theta^{(i+1)} = \frac{1}{2}\left(1 + \sqrt{1 + 4(\theta^{(i)})^2}\right)$
- $\mathbf{y}^{(i+1)} = \mathbf{x}^{(i)} + \left(\frac{\theta^{(i)} - 1}{\theta^{(i+1)}}\right)\left(\mathbf{x}^{(i)} - \mathbf{x}^{(i-1)}\right)$
- $i \leftarrow i + 1$

3.2. Scan patterns

The random scanning system implemented at LPS allows us to choose which pixel we want to sample. In what follows, three scan patterns will be proposed and their reconstruction quality will be discussed. The first proposed scan pattern is the random scan which consists in randomly acquiring N pixels over P. At the opposite side, we also consider a regular sampling, which produces a more uniform coverage of the sample. In between, we also consider a jittered scan which consists in randomly choosing a pixel among regularly distributed sub-grids. As an example, for $r = 0.25$, a pixel will be drawn among sub-grids of 2×2 pixels. These scan patterns will be discussed in subsection 4.3.

4. SIMULATION RESULTS

4.1. Synthetic datasets

The performances of the proposed methods are assessed thanks to experiments conducted on synthetic spectrum-images. More precisely, the full spectrum-image $\mathbf{Y} \in \mathbb{R}^{M \times P}$ is generated according to

$$\mathbf{Y} = \mathbf{X} + \mathbf{E} \tag{9}$$

where $\mathbf{X}$ is the noise-free spectrum image and $\mathbf{E}$ is a noise matrix. To mimic realistic EELS acquisitions, the noise-free image has been decomposed as $\mathbf{X} = \mathbf{M}\mathbf{A}$, following the so-called linear mixing model that can be used to describe the spatial mapping of materials within an observed sample [5]. The $M \times N_c$ matrix $\mathbf{M} = [\mathbf{m}_1, \ldots, \mathbf{m}_{N_c}]$ gathers N_c spectra associated with distinct materials (referred to as *endmembers*) and $\mathbf{A} = [\mathbf{a}_1, \ldots, \mathbf{a}_P]$ is a $N_c \times P$ matrix which stands for the spatial distribution of the materials in the pixels (referred to as *abundances*). Here, $N_c = 4$.

The endmember spectra have been extracted from reals EELS data using the vertex component analysis (VCA) [9]. The spectra are shown in Figure 1 where four particular energy thresholds reveal the presence of chemical elements: carbon (K-edge at 285 eV), calcium (L 2,3 -edge composed of a double peak around 350 eV), nitrogen (K-edge at 400 eV) and oxygen (K-edge at 530 eV). These components do not correspond to well defined chemicals compounds. Nevertheless, for simplicity, in the following, the endmembers will be related to particular materials and designed as calcification, resin, organic 1 and organic 2. The number of bands (corresponding to energy channels of the spectrometer) is M = 1337.

Concerning the four abundance maps $\mathbf{A}_{k,:} = [a_{k1}, \ldots, a_{kP}]$ ($k \in [\![1, N_c]\!]$) represented in Fig. 2 (first column) have been designed to define the spatial distribution of the different materials in the sample. In these experiments, the spatial maps are of size 100×100 pixels and sum exactly to 1.

4.2. Unmixing analysis of reconstructed data

In this section, the observation matrix $\mathbf{Y}_{\mathcal{I}}$ is generated using $r = 0.25$ (the scan pattern is chosen to be random here) and a signal-to-noise ratio of 25dB is chosen, corresponding to a classical non-destructive electron dose. Its 3S reconstruction quality is evaluated by comparing the 3S reconstruction (Reconstruction) to the noise-free spectrum-image (Oracle). The considered criterion is the normalized mean square error (NMSE) of the reconstructed image $\hat{\mathbf{X}}$

$$\text{NMSE}(\mathbf{X}, \hat{\mathbf{X}}) = \frac{||\hat{\mathbf{X}} - \mathbf{X}||_{\text{F}}^2}{||\mathbf{X}||_{\text{F}}^2}. \tag{10}$$

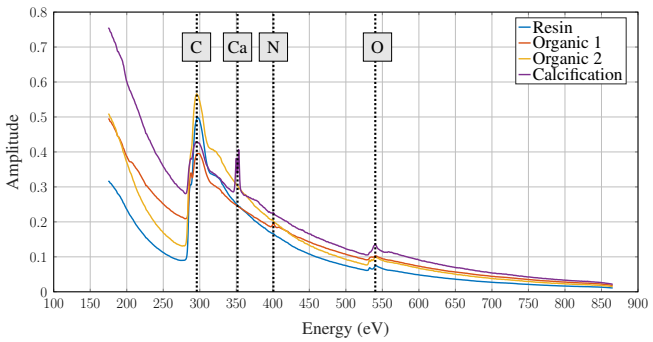

Fig. 1. The $N_c = 4$ endmember spectra represented as amplitude vs. energy loss (in eV). The following characteristic thresholds are depicted: carbon (285 eV), calcium (350 eV), nitrogen (400 eV) and oxygen (530 eV).

Standard unmixing techniques are also used to analyze the 3S reconstruction technique. Particularly, for both Oracle and Reconstruction spectrum-images, the spectra $\mathbf{m}_k$, $k \in [\![1, \ldots, N_c]\!]$, have been recovered using the SISAL algorithm [10] applied on the acquired data. Then, the abundance maps $\mathbf{A}$ are estimated from the compared images using the SUNSAL algorithm [11]. The quality of the estimated endmember matrix $\hat{\mathbf{M}}$ is evaluated using the average spectral angle distance (aSAD) defined by [12]

$$\text{aSAD}(\mathbf{M}, \hat{\mathbf{M}}) = \frac{1}{N_c} \sum_{k=1}^{N_c} \text{acos}\left(\frac{\langle \mathbf{m}_k, \hat{\mathbf{m}}_k \rangle}{||\mathbf{m}_k||_2 \times ||\hat{\mathbf{m}}_k||_2} \right). \tag{11}$$

The relevance of the estimated abundance maps is evaluated by computing the corresponding $\text{NMSE}(\mathbf{A}, \hat{\mathbf{A}})$ as defined by (10). Figure 2 shows the estimated abundance maps while the two first lines of Table 1 give the metric results These results show that Oracle and Reconstruction unmixing results are comparable and succeed in analyzing the sample elements.

4.3. Scan pattern impact

Here, the study detailed in previous subsection is conducted for the three scan patterns given in subsection 3.2. Their corresponding sampling masks are given in Figures 3(a) to 3(c), colored compositions of the reconstructed spectrum-images are given in Figures 3(d) to 3(f) and unmixing performances are given in Table 1. As expected, the random scan seems to give the worst results since the mask presents black holes. Regular and jittered scan patterns give quite similar performances but the regular reconstruction spectrum image contains artefacts, especially visible in only-resin areas.

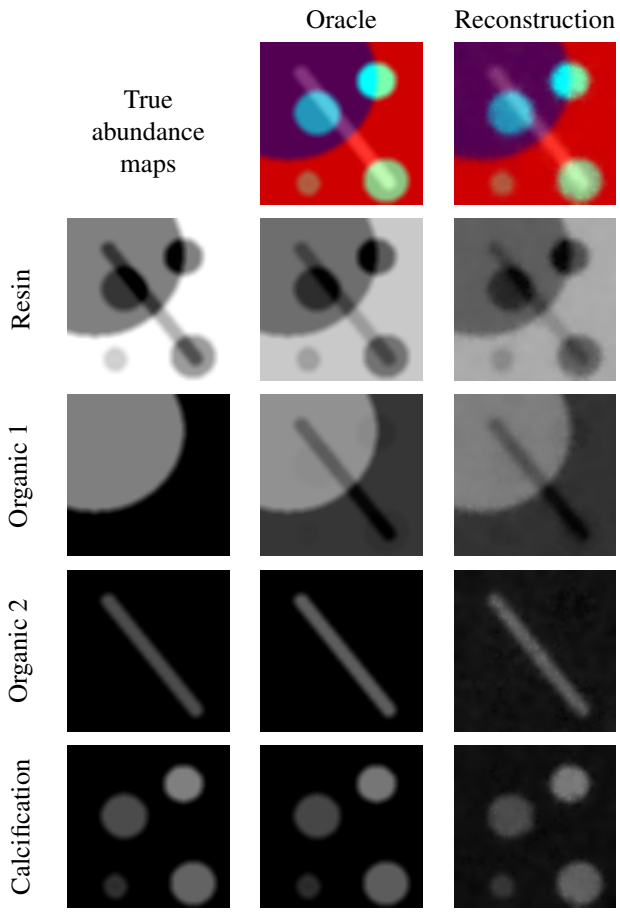

Fig. 2. Row 1: colored composition of the oracle and reconstructed spectrum-images. Rows 2-5: the abundance maps estimated by SUNSAL on the corresponding spectrum-images.

Table 1. Unmixing performance with respect to scan pattern.

Pattern	$\text{NMSE}(\mathbf{X}, \hat{\mathbf{X}})$	$\text{aSAD}(\mathbf{M}, \hat{\mathbf{M}})$	$\text{NMSE}(\mathbf{A}, \hat{\mathbf{A}})$
Oracle	0.00000	0.10254	0.33640
Random	0.00017	0.10315	0.51204
Regular	0.00010	0.11616	0.38726
Jittered	0.00013	0.09299	0.34585

5. A REAL DATA APPLICATION

In this section, the proposed reconstruction method is applied to a real spectrum-image acquired by the STEM VG HB 501 microscope and equipped with a partial sampling implementation. The acquired image size is 100×98 pixels and is composed of 1337 bands. Two protocols were applied to the same sample: a full sampling ($r = 1$) with a small local electron dose d (which gives the $\text{Full}_{2\text{ms}}$ image) and a partial sampling

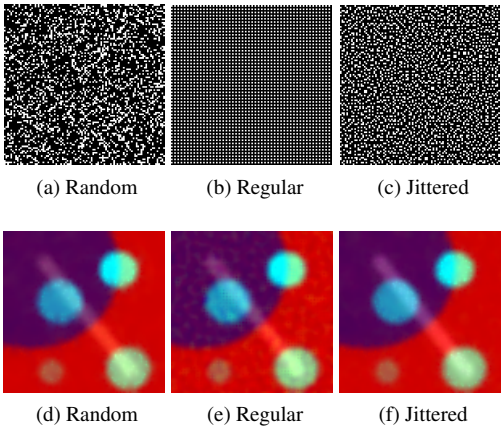

(a) Random (b) Regular (c) Jittered

(d) Random (e) Regular (f) Jittered

Fig. 3. Sampling masks (a)-(c) and the reconstructed spectrum images colored compositions (d)-(f) for random, regular and jittered scan patterns.

($r = 0.2$) with a higher local electron dose $5d$ (Reconstruction image). An unmixing study using the VCA algorithm followed by the SUNSAL algorithm has been conducted on both images. The three most powerful maps are given in Figure 4. We can observe that our approach returns abundance maps similar to the ones returned by standard acquisition scheme and a denoing action is observed.

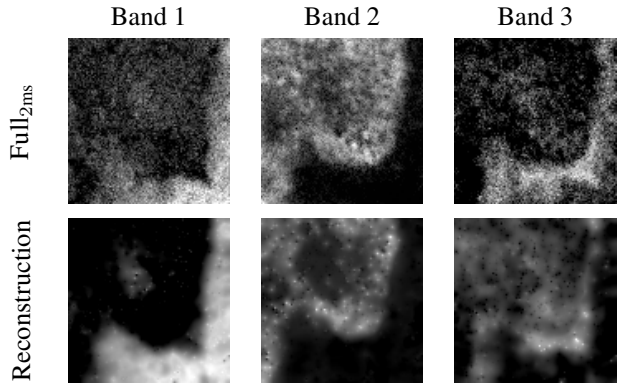

Fig. 4. The abundance maps estimated by SUNSAL applied to the two real spectrum-images $\text{Full}_{2\text{ms}}$ and Reconstruction.

6. CONCLUSION

In this paper, we introduced new acquisition and reconstruction techniques to better preserve sensitive materials in scanning transmission electron microscopy. The proposed method is based on a partial acquisition of an EELS spectrum-image followed by reconstruction using a priori information. An algorithm was proposed to conduct the reconstruction task and experiments compared this approach with a standard acquisition scheme.

When comparing with a standard (full) acquisition, the partial sampling scheme showed better spectra estimation, while some spatial details seemed deteriorated. Note that there are other benefits of partial sampling, including a better distribution of the energy within the sample, and the ability of reconstructing dynamic (temporal) sequences. This opens new perspectives towards fast or dynamic STEM-EELS imaging.

7. REFERENCES

[1] R. F. Egerton, *Electron Energy-Loss Spectroscopy in the Electron Microscope*. New York: Springer, 2011.

[2] R. F. Egerton, P. Li, and M. Malac, "Radiation damage in the TEM and SEM," *Micron*, vol. 35, no. 6, pp. 399–409, 2004.

[3] A. Béché, B. Goris, B. Freitag, and J. Verbeeck, "Development of a fast electromagnetic beam blanker for compressed sensing in scanning transmission electron microscopy," *Appl. Phys. Lett.*, vol. 108, no. 9, pp. 093 103–1–093 103–5, Feb. 2016.

[4] A. Tararan, M. Tencé, N. Brun, M. Kociak, and A. Zobelli, "Random scanning mode for the spectroscopy of sensitive materials," in *Proc. Eur. Microsc. Congr.*, 2016.

[5] N. Dobigeon and N. Brun, "Spectral mixture analysis of EELS spectrum-images," *Ultramicroscopy*, vol. 120, pp. 25–34, 2012.

[6] E. Monier, T. Oberlin, N. Brun, M. Tencé, M. de Frutos, and N. Dobigeon, "Reconstruction of partially sampled multi-band images – Application to EELS microscopy," submitted. [Online]. Available: http://arxiv.org/abs/1802.10066/

[7] S. P. Lin and M. D. Perlman, "A Monte Carlo comparision of four estimators for a covariance matrix," in *Multivariate Anal.*, vol. 6, 1985, pp. 411–429.

[8] A. Beck and M. Teboulle, "A fast iterative shrinkage-thresholding algorithm for linear inverse problems," *SIAM J. Imag. Sci.*, vol. 2, no. 1, pp. 183–202, Jan. 2009.

[9] J. M. P. Nascimento and J. M. Bioucas-Dias, "Vertex component analysis: a fast algorithm to unmix hyperspectral data," *IEEE Trans. Geosci. Remote Sens.*, vol. 43, no. 4, pp. 898–910, April 2005.

[10] J. M. Bioucas-Dias, "A variable splitting augmented Lagrangian approach to linear spectral unmixing," in *Proc. IEEE GRSS Workshop Hyperspectral Image SIgnal Process.: Evolution in Remote Sens. (WHISPERS)*, 2009, pp. 1–4.

[11] J. M. Bioucas-Dias and M. A. T. Figueiredo, "Alternating direction algorithms for constrained sparse regression: Application to hyperspectral unmixing," in *Proc. IEEE GRSS Workshop Hyperspectral Image SIgnal Process.: Evolution in Remote Sens. (WHISPERS)*, 2010, pp. 1–4.

[12] N. Keshava, "Distance metrics and band selection in hyperspectral processing with applications to material identification and spectral libraries," *IEEE Trans. Geosci. Remote Sens.*, vol. 42, no. 7, pp. 1552–1565, 2004.